Journal Pre-proof

Wear rate at RT and 100□°C and operating temperature range of microalloyed $Cu_{50}Zr_{50}$ shape memory alloy

A. Younes, P. Nnamchi, J. Medina, P. Pérez, Victor M. Villapún, F. Badimuro, S. Kamnis, E. Jimenez-Melero, S. González

PII: S0925-8388(19)34576-1

DOI: https://doi.org/10.1016/j.jallcom.2019.153330

Reference: JALCOM 153330

To appear in: *Journal of Alloys and Compounds*

Received Date: 12 October 2019

Revised Date: 3 December 2019

Accepted Date: 7 December 2019

Please cite this article as: A. Younes, P. Nnamchi, J. Medina, P. Pérez, V.M. Villapún, F. Badimuro, S. Kamnis, E. Jimenez-Melero, S. González, Wear rate at RT and 100□°C and operating temperature range of microalloyed $Cu_{50}Zr_{50}$ shape memory alloy, *Journal of Alloys and Compounds* (2020), doi: https://doi.org/10.1016/j.jallcom.2019.153330.

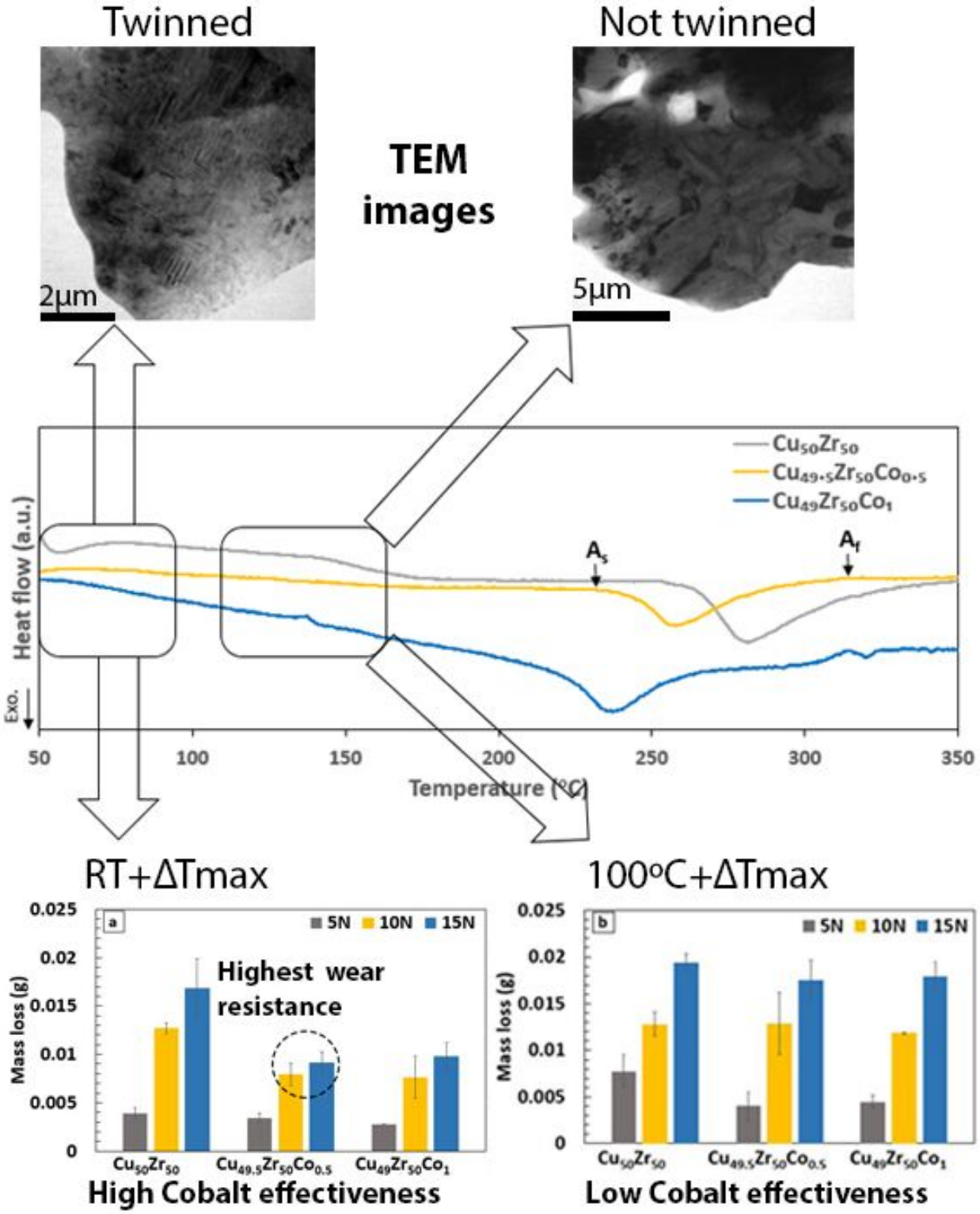
Twinned
Not twinned
TEM images
2μm
5μm
Heat flow (a.u.)
Exo.
Temperature (°C)
$Cu_{50}Zr_{50}$
$Cu_{49.5}Zr_{50}Co_{0.5}$
$Cu_{49}Zr_{50}Co_{1}$
A_s
A_f
RT+ΔTmax
100°C+ΔTmax
Mass loss (g)
5N
10N
15N
Highest wear resistance
High Cobalt effectiveness
Low Cobalt effectiveness

Wear rate at RT and 100°C and operating temperature range of microalloyed $Cu_{50}Zr_{50}$ shape memory alloy

A. Younes[a], P. Nnamchi[a], J. Medina[b], P. Pérez[b], Victor M. Villapún[a], F. Badimuro[c], S. Kamnis[d], E. Jimenez-Melero[e], S. González[a]

[a]Faculty of Engineering and Environment, Northumbria University, Newcastle upon Tyne NE1 8ST, UK
[b]Centro Nacional de Investigaciones Metalúrgicas, CSIC, Avda. Gregorio del Amo 8, 28040 Madrid, Spain
[c]School of Chemical and Process Engineering, University of Leeds, Leeds LS2 9JT, UK
[d]Monitor Coatings, Tyne and Wear, UK
[e]Materials Performance Centre, School of Materials, University of Manchester, M13 9PL, UK

Abstract

The effect of microalloying with Co on the wear rate and on the operating temperature range of $Cu_{50}Zr_{50}$ shape memory alloy against 304 stainless steel counterface has been investigated by studying the mass loss and wear behaviour of $Cu_{50}Zr_{50}$, $Cu_{49.5}Zr_{50}Co_{0.5}$ and $Cu_{49}Zr_{50}Co_1$ at. % at room temperature (RT) and 100^{o}C. For the alloys tested at 15N, maximum wear resistance is achieved at RT for the alloy with 0.5 at. % Co compared to the parent $Cu_{50}Zr_{50}$ at. % alloy. This is mostly attributed to the effect of Co in promoting stress-induced martensitic transformation (i.e., work-hardening). For wear tests at 100°C (100^{o}C plus friction temperature for 1 hour), the mass loss is higher than that at RT since martensite partly reverts into soft austenite through an isothermal process. In addition, the alloys are more prone to oxidation with formation of thick oxide layers that can easily get fragmented and detached from the surface thus resulting is higher mass loss than at RT. The effect of Co in promoting martensitic transformation is negligible when testing at 100^{o}C, since the stress-induced martensite partly reverts into austenite and the thick oxide layer formed on the surface not only masks the effect of the underlaying substrate for it can also easily detach upon wear.

Keywords: Metals and alloys; Quenching; Shape memory; Mechanical properties

1. Introduction

The interest in using shape memory alloys (SMAs) stems from the fact that they “remember” their original shape. When subjected to an external force high enough to plastically deform the material, they exhibit stress-induced martensitic transformation

where metastable austenite transforms into martensite. Afterwards, when heated above certain temperature [1], they can recover the apparent permanent strains and return to its original form. Traditionally, nitiol (i.e., NiTi) has been used as shape memory alloy due to its high specific work output [2]. For this reason it is a potential candidate alloy for multiple applications but it is relatively expensive due to the high cost associated to the element titanium. In this regard, CuZr based shape memory alloys are good candidates because their cost is lower [3] than that of NiTi alloy but their performance is also lower. For this reason, an important topic of research is how to improve the shape memory behaviour of CuZr alloys to render higher cost-effectiveness. It is known that the mechanical performance of SMAs depends on their microstructure [4-6] and this can be tuned through control of the cooling rate and heat treatment. The composition also plays an important role on the microstructure. For example, it was found [5] that minor change in Cu content in the range of ±2% at.% in CuZr system strongly influences the microstrcutre in terms of presence of intermetallics such as $CuZr_2$ and $Cu_{10}Zr_7$ and their volume fraction in the overall alloys.

Traditionally, rapidly solidified materials can be used as precursor to tune the microstructure upon cooling and annealing. The microstructure can also be tailored directly upon cooling. For example, a decrease in the cooling rate could promote the formation of intermetallic phases [7] and change the relative volume fraction of austenite, martensite and intermetallic phases, such as the case for [7] where variation of cooling rate resulted on difference in mechanical performance as well as greatly influencing the martensitic transformation temperature.

The addition of an alloying element, such as Co, at different concentrations may stabilize one phase over the other [8]. When the alloying element is in small concentrations (i.e., microalloying) it can reduce the stacking fault energy of the crystalline austenite B2-CuZr phase, enhancing the twinning propensity and thus favouring the martensitic transformation into martensite B19’ CuZr upon mechanical loading [9]. Since martensite is harder than austenite and the wear resistance is proportional to H/Er [10], the wear resistance would increase with increasing martensite content [11]. The transformed martensite can subsequently revert to the original pre-deformed austenite phase when subjected to post-deformation annealing. The stress-induced martensitic transformation can be promoted through

accurate control of the nature and concentration of microalloying element/s [9]. For example, partial replacement of Cu by minor concentration of Ni, Co and Fe decreases the stress required to transform B2 CuZr austenite into B19' CuZr martensite, with Co being the element that most effectively decreases the stacking fault energy of austenite as was experimentally [9, 12, 13] and theoretically proven [14]. Other microalloying elements can induce different effects, for example, for $Cu_{48}Zr_{48-x}Al_4Nb_x$ where $x \leq 2$ at. % [15] Nb addition enhances the yield strength of the base alloy by 20% and the tensile plasticity by about 8 %. This superior mechanical behaviour is attributed to the combination of the formation of multiple shear bands and martensitic transformation of B2 CuZr phase. The addition of microalloying elements can also have an effect on the glass forming ability and therefore on the alloy microstructure. For example, addition of 0.5 at. % Ta to CuZr-based alloys promotes the formation of crystalline B2 CuZr upon cooling [16].

Although there is a relatively large number of studies Cu-based SMAs showing improvement in mechanical properties, [17-19] and number of papers studied the wear performance of SMAs at room temperature (RT), the knowledge about the wear performance at higher testing temperatures is scarce. This is relevant since the temperature at which engineering components operate may vary during the work period and therefore the tribological performance will vary as well. For example, industrial electric motors can reach about 100^{o}C and surfaces under full sunlight in space can go beyond that temperat17ure. For this reason, the wear behaviour of the SMAs have been studied at room temperature (RT) and at 100^{o}C. Moreover, considering that the mechanical behaviour of CuZr SMAs can be tuned through microalloying [9, 12, 13, 20] but they have not been explored at temperatures higher than RT before, the tribological properties at both temperatures will be studied. This research is therefore expected to shed light on the tribological performance of SMAs in microactuators for satellites and motors.

2. Experimental

Alloy ingots of nominal composition $Cu_{50}Zr_{50}$, $Cu_{49.5}Zr_{50}Co_{0.5}$, and $Cu_{49}Zr_{50}Co_1$ alloys (at. %) were prepared from elements with purity higher than 99.9 at. %. The master alloys were remelted three times in a Ti-gettered high purity argon atmosphere to attain good chemical homogeneity using Compact Arc Melter MAM-1 Edmund

Bühler. Rod samples of 3 mm in diameter were obtained from the master alloy by copper mould casting in an inert gas atmosphere. The structure of the as-cast samples was studied by X-ray diffraction (XRD) using a Phillips Panalytical X'Pert Pro MPD diffractometer with non monochromated Cu Kα_radiation (step size 0.03°). The thermal behaviour of the samples was studied using differential scanning calorimetry (DSC, SETARAM C131 EVO) at a constant heating rate of 5 K/min up to 550°C and natural cooling rate inside the furnace down to room temperature. The microstructure was investigated by scanning and transmission electron microscopy (SEM and TEM respectively). Dry sliding wear experiments were conducted using a pin-on disc (DUCOM Micro POD) in air at room temperature and at 100°C following the ASTM-G99. The pins were made using the as-casted rods and their surfaces were mirror surface polished using 4000 grit paper prior to wear testing against a counterbody disc of 60 HRC hardened SS304 stainless steel of 0.6 µm (Ra) surface roughness provided by the company DUCOM. Tests were performed at increasing loads of 1, 5, 10 and 15 N at a sliding velocity of 0.5 m/s for a sliding distance of 1800 m. The mass loss was obtained by measuring the weight of the pins before and after the wear tests using an analytical balance (Fisherbrand™ Analytical Balance, ±0.1mg). Surface roughness was measured using an Alicona profilometre from an average of 10 lines perpendicular to the surface profile.

3. Results and discussion

3.1. Microstructural characterization of the as-cast pins

Fig. 1 shows the XRD patterns for $Cu_{50}Zr_{50}$, $Cu_{49.5}Zr_{50}Co_{0.5}$ and $Cu_{49}Zr_{50}Co_1$ at. % alloys. The crystalline phases detected are orthorhombic $Cu_{10}Zr_7$ (a = 0.9347 nm, b = 0.9347 nm, c = 1.2675 nm), orthorhombic Cu_8Zr_3 (a = 0.78686 nm, b = 0.81467 nm, c = 0.9977 nm), austenite B2 CuZr (a = 3.2562 nm, b = 3.2562 nm, c = 3.2562 nm), monoclinic martensite B19' CuZr (a = 0.3237 nm, b = 0.4138 nm, c = 0.5449 nm) and tetragonal $CuZr_2$ (a = 0.3220 nm, b = 0.3220 nm, c= 1.1183 nm). In addition, the small overlapping halo indicates the presence of a fine microstructure, which is consistent with the TEM analysis (see section 3.7). The main peak at around $2\theta = 39.4^o$ corresponds to B2 CuZr austenite and its intensity is smaller for the alloys containing Co (Fig. 1a, 1b and 1c). Multiple peaks associated with martensite are detected at around 36.5° and 56.5°, while other peaks overlap with

peaks corresponding to the intermetallic phases (Cu_8Zr_3, $Cu_{10}Zr_7$ and $CuZr_2$). Consequently, a mixture of austenite, martensite and intermetallic phases are present in different proportions upon quenching for the three compositions. The small halos detected between 35 to 45°C corresponds to the overlapping of XRD peaks associated to a fine microstructure as can be observed in section 3.7.

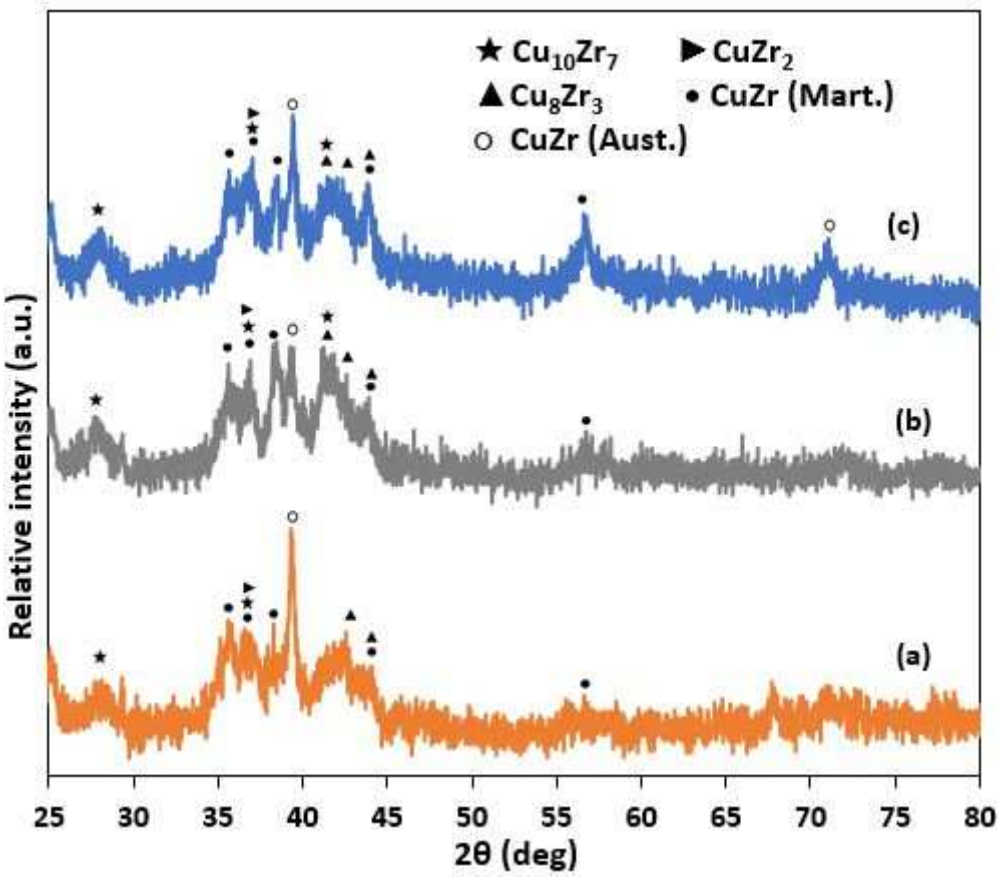

Fig. 1. XRD scan of as cast (a) $Cu_{50}Zr_{50}$, (b) $Cu_{49.5}Zr_{50}Co_{0.5}$ and (c) $Cu_{49}Zr_{50}Co_1$ alloys.

To understand the mechanical behaviour of $Cu_{50}Zr_{50}$, $Cu_{49.5}Zr_{50}Co_{0.5}$ and $Cu_{49}Zr_{50}Co_1$ alloys at RT and at 100°C, wear tests will be conducted at both temperatures (see section 3.2) and therefore their thermal behaviour will be first studied by DSC (Fig. 2). Upon heating, a large exothermic peak associated with the transformation of martensite into austenite is detected and the temperatures at which the transformation starts A_s and ends, A_f, are listed on Table 1. This peak shifts towards lower temperatures with increasing Co content: Co_0 (curve a: A_s = 256.3 and A_f = 340.7°C), $Co_{0.5}$ (curve b: A_s = 235.2 and A_f = 312.3°C) and Co_1 (curve c: A_s = 218.8 and A_f = 268.9°C), indicating that addition of Co tends to stabilize the formation of austenite [13] thermodinamically upon cooling [21, 22]. When the molten

alloy start to cool down during the casting process, certain phases stabilizse at different temperatures [23], in this case, the addition of Co in solid solution tend to stabilise B2 CuZr austenite [24].

It is well known that martensite is harder and more wear resistant than austenite and therefore it is of interest to prevent the temperature to surpass A_s. For this reason it is important for engineering components subjected to wear to work within the operational temperature range, A_s-RT, and in this work the range decreases from 236.3°C for Co_0 to 215.2°C for $Co_{0.5}$ and 198.8°C for Co_1 alloy (see Table 1).

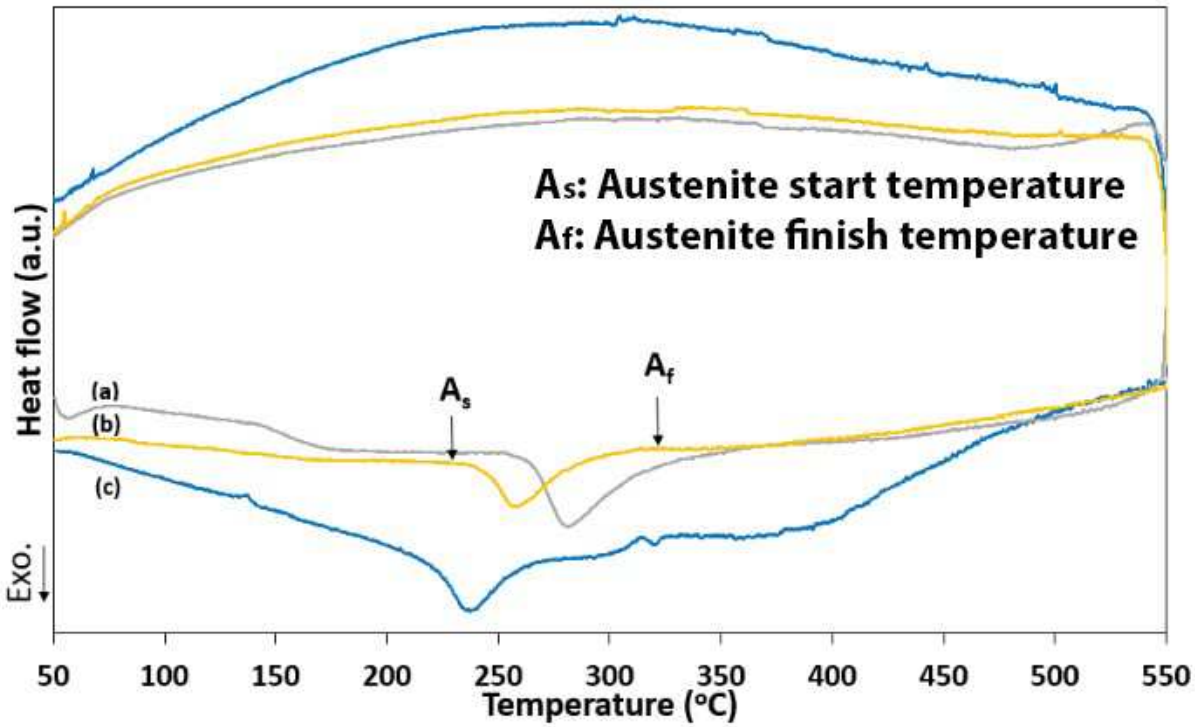

Fig. 2. DSC curves for (a) $Cu_{50}Zr_{50}$, (b) $Cu_{49.5}Zr_{50}Co_{0.5}$ and (c) $Cu_{49}Zr_{50}Co_1$ heated up at 5K/min up to 550°C and left to cool down naturally in the DSC.

Table 1. Transformation temperatures for the three compositions and operational temperature range.

Composition (at. %)	A_s (°C)	A_f (°C)	Operational temperature range A_s-RT (°C)
$Cu_{50}Zr_{50}$	256.3	340.7	236.3
$Cu_{49.5}Zr_{50}Co_{0.5}$	235.2	312.3	215.2
$Cu_{49}Zr_{50}Co_1$	218.8	268.9	198.8

3.2. Wear tests

Fig. 3 shows the evolution of the mass loss for 3 mm diameter $Cu_{50}Zr_{50}$, $Cu_{49.5}Zr_{50}Co_{0.5}$ and $Co_{49}Zr_{50}Co_1$ (at. %) rods tested at 5, 10 and 15 N load for 1h at two different conditions, room temperature (RT) (Fig. 3a) and 100°C (Fig. 3b).

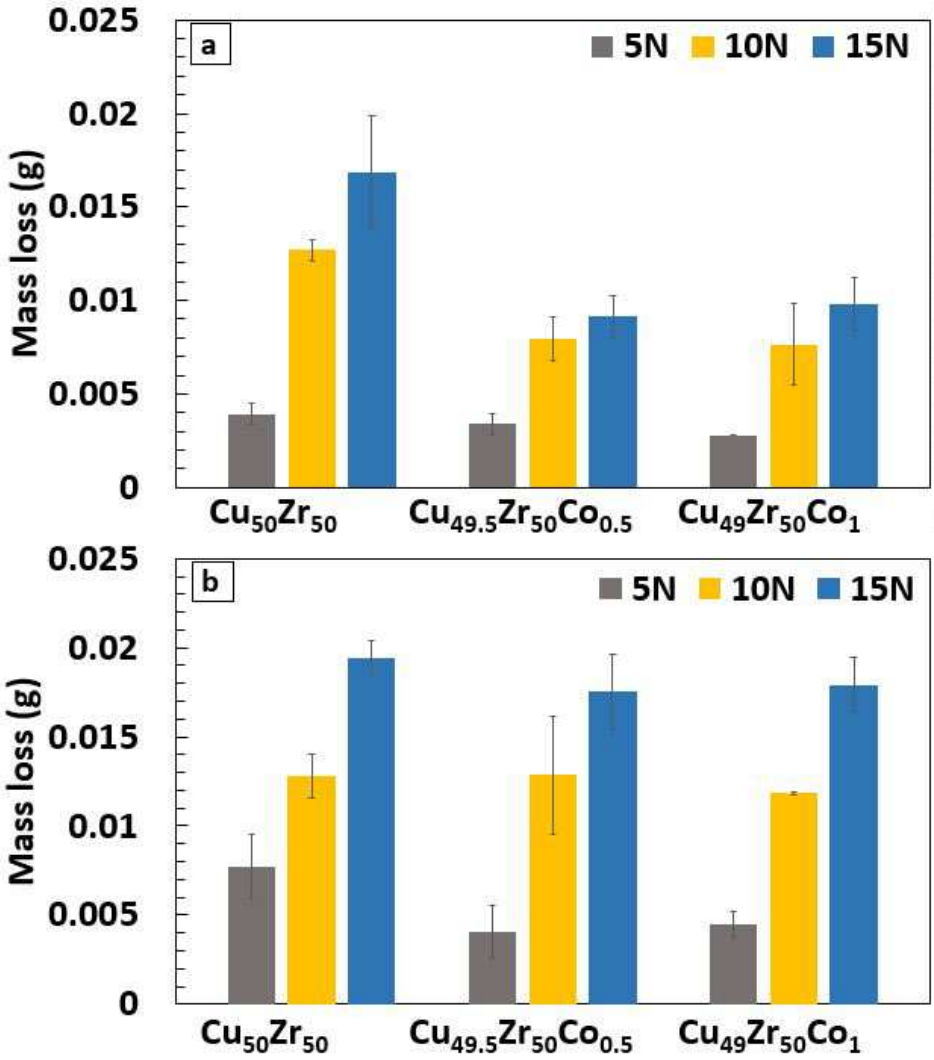

Fig. 3. Mass loss for $Cu_{50}Zr_{50}$, $Cu_{49.5}Zr_{50}Co_{0.5}$, and $Cu_{49}Zr_{50}Co_1$ alloys tested at 5, 10 and 15 N load for 1 h at a) room temperature and b) 100°C.

Table 2. Code for the different compositions and testing conditions of load and temperature.

Load (N)	Composition (at. %)					
	$Cu_{50}Zr_{50}$		$Cu_{49.5}Zr_{50}Co_{0.5}$		$Co_{49}Zr_{50}Co_1$	
	Room Temperature (RT)	100°C	Room Temperature (RT)	100°C	Room Temperature (RT)	100°C
5	$5NCo_0RT$	$5NCo_0100^oC$	$5NCo_{0.5}RT$	$5NCo_{0.5}100^oC$	$5NCo_1RT$	$5NCo_1100^oC$
10	$10NCo_0RT$	$10NCo_0100^oC$	$10NCo_{0.5}RT$	$10NCo_{0.5}100^oC$	$10NCo_1RT$	$10NCo_1100^oC$
15	$15NCo_0RT$	$15NCo_0100^oC$	$15NCo_{0.5}RT$	$15NCo_{0.5}100^oC$	$15NCo_1RT$	$15NCo_1100^oC$

These tests have been coded according to the composition and testing conditions (load and temperature) as listed in Table 2. For RT tests, a clear trend of mass loss increase with increasing load is observed, and it is maximum for $Cu_{50}Zr_{50}$ at. % ranging from about 0.0039 g for 5 N to about 0.0169 g for 15 N. The average mass loss has increased about 33% when the load increases from 10 N ($10NCo_0RT$) to 15 N ($15NCo_0RT$). Smaller mass losses are detected for the Co-containing alloys than for $Cu_{50}Zr_{50}$ at. % and especially at 15 N load for the alloy with 0.5 at. % Co since the mass loss for $Co_{0.5}$ (0.0091 g) is smaller than for Co_0 (0.017 g) and Co1 (0.0098 g). At 100°C (Fig. 3b), the mass loss is generally higher than at RT, especially at high loads for the Co-containing alloys. The effect of the composition seems less significant than for tests at RT since similar increases in mass loss are found for the three compositions when the applied load is increased. The mass loss increases by 52%, 36 and 51%, when the applied load is raised from 10 to 15 N for Co_0, $Co_{0.5}$ and Co_1, respectively. The mass loss difference is slightly more noticeable at 15 N, with a maximum mass loss of about 0.0194, 0.0175 and 0.0179 g for Co_0, $Co_{0.5}$ and Co_1, respectively. The mass loss values are higher at 100°C than at RT while the evolution of the mass loss with increasing Co content is more noticeable at RT than at 100°C. This suggests that any mechanism responsible for the deformation associated with microalloying (i.e., twinning propensity) has little effect at 100°C. In fact, for 15 N load, the decrease in mass loss from $15NCo_0RT$ to $15NCo_{0.5}RT$ is about 46 % while it is only about 10 % between $15NCo_0100$°C and $15NCo_{0.5}100$°C.

It should be noted that the mechanism responsible for stabilization of austenite with Co addition upon cooling (see DSC in Fig. 3), is different from the mechanism responsible for stress-induced martensitic transformation. Microalloying with $Co_{0.5}$ is

shown to promote stress-induced martensitic transformation due to the fact that the newly formed B2 CuZr with Co in solid solution has lower stalking fault energy than that of the parent alloy [9].

3.3. Microstructural analysis after wear tests

In order to understand the evolution of the wear performance on the surface of tested samples, In-beam Secondary Electron (SE) SEM images have been taken for all the compositions at 10 and 15 N at RT and 100^{o}C as shown in (Fig. 4).

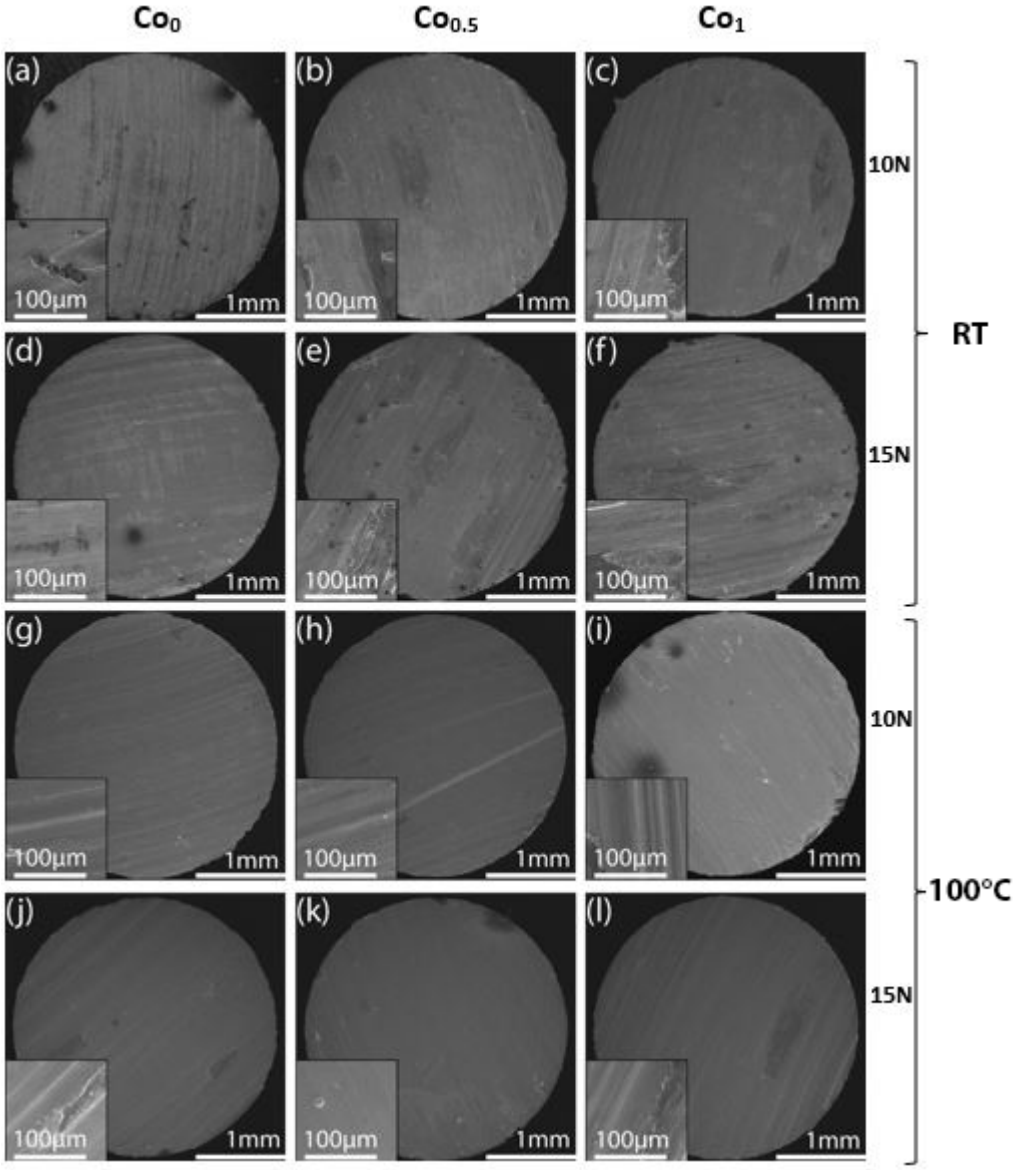

Fig. 4. In-beam Secondary electron (SE) SEM images for a) 10NCo$_0$RT b) 10NCo$_{0.5}$RT c) 10NCo$_1$RT d) 15NCo$_0$RT e) 15NCo$_{0.5}$RT f) 15NCo$_1$RT g) 10NCo$_0$100^{o}C h) 10NCo$_{0.5}$100^{o}C i) 10NCo$_1$100^{o}C j) 15NCo$_0$100^{o}C k) 15NCo$_{0.5}$100^{o}C l) 15NCo$_1$100^{o}C pin samples. Insets: magnified image from a representative area of the pin.

The surface finish for samples tested at RT show surface features and grooves originated from the wear process with the disc, this clear pattern of grooves is not as clear for samples tested at 100^{o}C. At higher temperature, the oxidation rate is increased, which leads to a thicker oxide layer that covers up the substrate pattern and features (see Fig. 4 g-l). The thicker oxide that was built at 100^{o}C, leads to higher removal rate as brittle oxides can easily get fragmented and detached, which could explain the higher mass loss for 100^{o}C compared to the behaviour at RT (Fig. 3). This is in line with the thickness of oxide layer study (see section 3.5). In order to investigate the different features in more detail, high magnification SEM images (see insets of Fig. 4) have been shown. All the surfaces show the presence of continuous grooves with material displaced to the lateral sides, thus suggesting that ploughing is the mechanism responsible for abrasive wear. The surface finish of tested samples contain different features that can be studied, samples tested at 100^{o}C exhibit abrasive wear and higher oxidation compared to samples tested at RT. For this reason, these features have been observed when testing at 100°C (i.e., SEM images of Fig. 5a and 5b for 15NCo$_0$100^{o}C). Fig. 5 shows the SEM images and corresponding EDX scans of two different representative areas from the surface of 15NCo$_0$100^{o}C sample. An elongated smeared patch of 500 μm long oriented along the groove direction is observed (Fig. 5a). According to EDX analysis the composition of these patches is 59.69 at. % Fe, 17.06 at. % Cr, 8.64 at. % Ni, 6.26 at. % O, 4.47 at. % Cu, 3.25 at. % Zr, 0.63 at. % Si, very rich in iron, oxygen, nickel, and chromium and therefore could correspond to the steel transferred from the disk onto the surface of the pin. Along with the patches there are small particles of dark tonality of about 44 μm (Fig. 5b) distributed homogeneously across the surface of the samples. EDX analysis of the particles indicate that their composition is 68.85 at. % O, 14.68 at. % Cu, 16.47 at. % Zr and therefore could be attributed to an oxidized debris released from the pin during the wear tests.

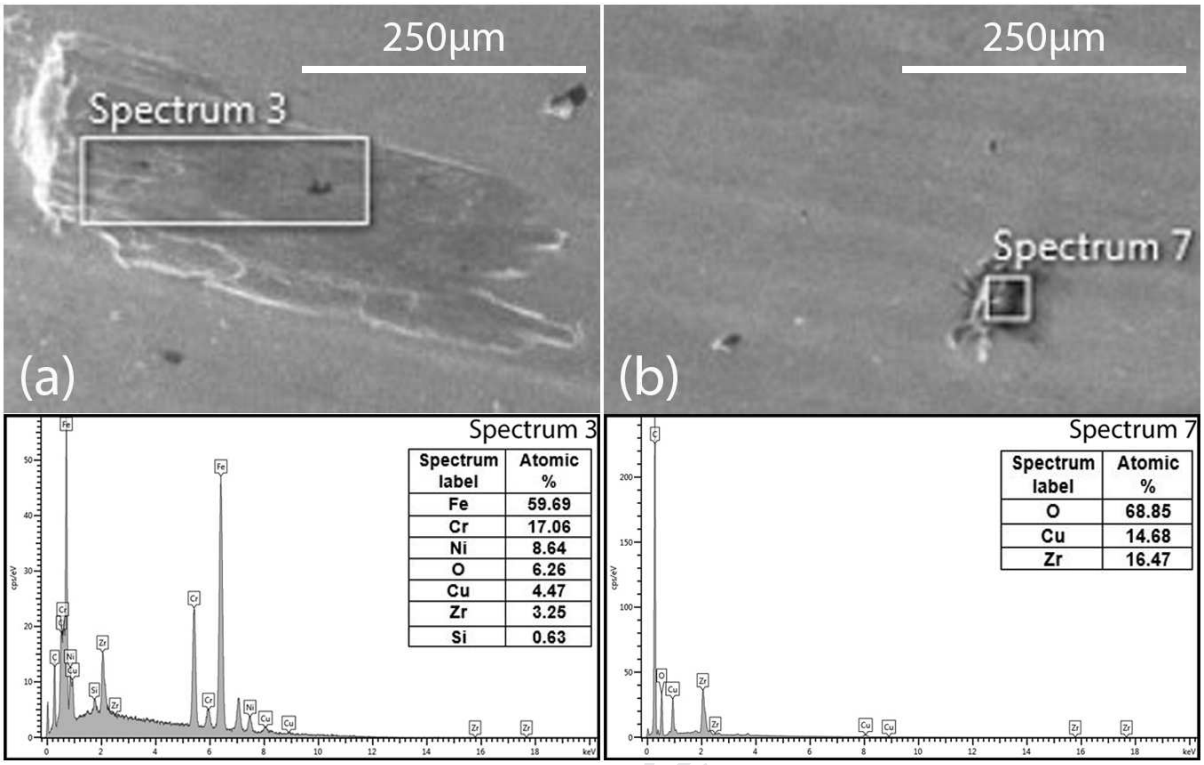

Fig. 5. SEM images and corresponding EDX scans showing two selected areas a) and b) from the surface of $15NCo_0100^oC$ sample.

The wear behaviour of the alloys not only depends on their as-cast microstructure and composition but also on the changes that take place on the surface of contact with the disc and microstructural changes over the wear test time. Considering that the Co_1 alloy is the most critical since it decreases the operating temperature range the most, the XRD scans for this alloy have been performed (Fig. 6) for the as-cast sample (Fig. 6a), for $15NCo_1100^oC$ from the bulk (Fig. 6b) and after annealing at 400°C for 1 h (Fig. 6c). XRD after annealing at 400^oC show that all martensite has transformed into austenite since the temperature is well beyond A_f = 268.9°C. The relative intensity of austenite peaks from the bulk of $15NCo_1100^oC$ (Fig. 6b) is intermediate between that in the as-cast condition (Fig. 6a) and after the transformation (A_f) (Fig. 6d) and therefore partial isothermal transformation from martensite into austenite has taken place.

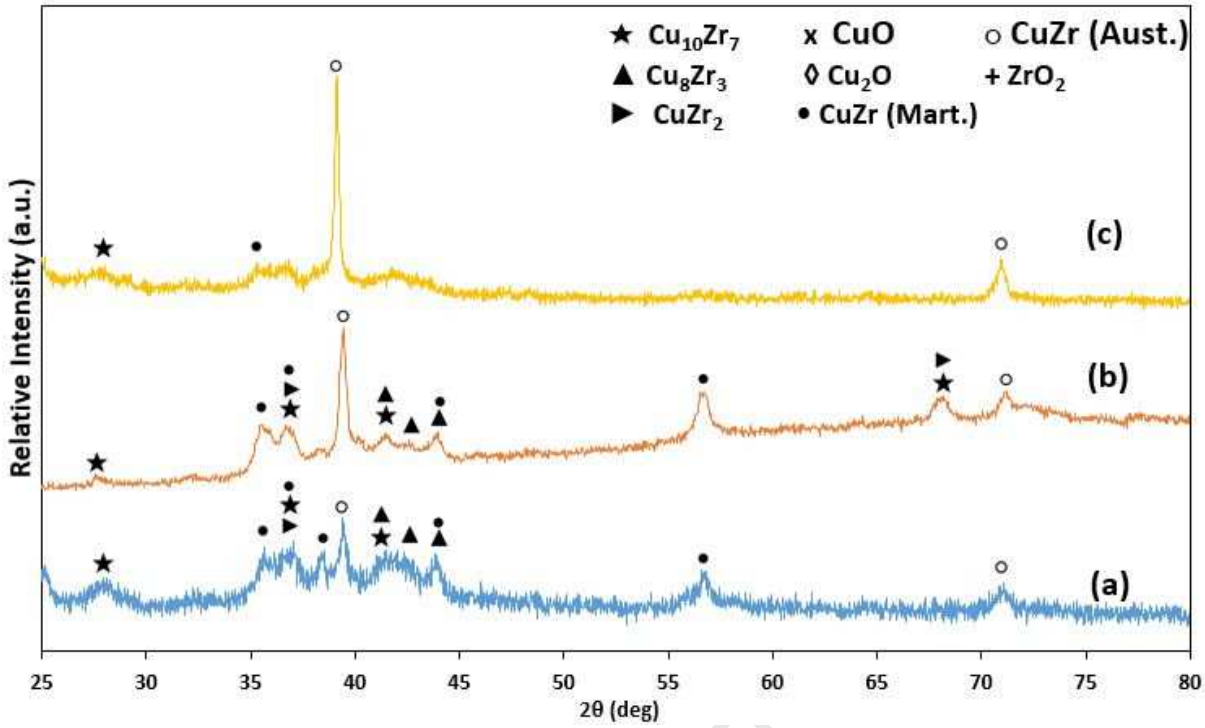

Fig. 6. XRD scans for the $Cu_{49}Zr_{50}Co_1$ alloy a) in the as-cast condition, b) after $15NCo_1100^oC$ wear test and (c) annealed at 400°C for 1 h.

3.4. Estimation of temperature rise at the pin/disk contact surface

The presence of oxides clearly suggests that friction between pin and disc can rise the temperature. The temperature rise at the centre of contact area between the pin and the disk can be estimated using the following friction temperature (ΔT_{max}) equation [25]:

$$\Delta T_{max} = \frac{1.31 b \mu p V}{\sqrt{\pi}(K_1\sqrt{1.2344+Pe_1}+K_2\sqrt{1.2344+Pe_2})} \quad (1)$$

where b, μ, p, V, K and Pe are the contact radius, friction coefficient, normal pressure, sliding velocity, thermal conductivity and the Peclet number respectively and assuming that material 1 is the rotating steel disk while material 2 is the stationary pin. Some of these parameters are calculated using the equations 3-8 given by [25] and these values have been subsequently substituted into Equation 1.

$$b = \left(\frac{3wr}{4E'}\right)^{\frac{1}{3}} \quad (2)$$

$$E' = \frac{1-\nu_1^2}{E_1} + \frac{1-\nu_2^2}{E_2} \quad (3)$$

$$r = \left(\frac{1}{R_{Pin}} + \frac{1}{R_{disk}}\right)^{-1} \quad (4)$$

$$Pe_1 = \frac{V_1 b \rho_1 1 C_1}{2K_1} \quad (5)$$

$$Pe_2 = \frac{V_2 b \rho_2 1 C_2}{2K_2} \quad (6)$$

$$p = \frac{w}{\pi b^2} \quad (7)$$

Where b, w, r, E' and p are the radius of contact circle, normal load, effective radius, effective modulus and pressure. The mechanical properties of the different alloys has been estimated using the rule of mixtures [26] given by:

$$M^{-1} = \Sigma f_i . M_i^{-1} \quad (8)$$

Table 3 lists mechanical properties of Cu, Zr, Co, steel disk, $Cu_{50}Zr_{50}$, $Cu_{49.5}Zr_{50}Co_{0.5}$ and $Cu_{49}Zr_{50}Co_1$ as well as the surface temperature at the centre of contact area between the pin and disk for the different loads (i.e. 5, 10 and 15N). For tests conducted at RT (20°C) and at 100°C, the temperature rise ΔT_{max} has been added. Values of ρ, K and C for Cu, Co and SS304 were taken from [27], K and C for Zr from [28] while ρ for Zr was interpolated from [29] using the rule of mixtures (see Equation 9). Young's modulus E and Poisson's ratio ν for Cu and Zr was taken from [12] and for Co and SS304 from [30] and [31] respectively. The value of E at 100°C can be calculated from [32]:

$$\frac{E}{E_0} = \left(1 - a\left(\frac{T}{T_m}\right)\right) \quad (9)$$

Where E is the Young's modulus at temperature T, E_0 is the modulus at 0 K and T_m is melting temperature. The constant "a" relates to the proportionality constant, which is around 0.5 due to the linear decrease of modulus from 0 K to melting temperature [32]. In addition, Poisson's ratio change with temperature is minimal [33] and practically has no effect in the estimation of temperature. From all these values, the friction temperatures (ΔT_{max}) have been calculated, added to the testing temperatures (RT or 100°C) and the resultant contact surface temperatures obtained and listed (Table 3). Additionally, the temperature measured experimentally using a thermocouple attached to the other side of the pin recorded a slightly lower temperature. This difference in temperature is attributed to the fact that contact surface temperature at the centre of the interaction between pin and disc is higher than the temperature measured at the other side of the pin despite the alloy being a

very heat conductive. The contact temperature increases with increasing load, as expected, due to the increase in friction temperature and achieve maximum values for 15 N at RT with 81°C for Co_0 and $Co_{0.5}$ while for Co_1 it is 78°C.

For 15 N load at 100°C the contact surface temperatures are 153°C for Co_0, 154°C for $Co_{0.5}$ and 155°C for Co_1 alloys. These results indicate that the contact surface temperature is always below the austenitic transformation temperature A_s (Fig. 2 and Table 1). These are, however, estimated values since there are uncertainties for calculation of ΔT_{max}, especially when obtaining the thermal conductivity for the three alloys. Thermal conductivity K of each individual element (i.e., Cu, Zr and Co) is well-known, however, several studies disagree on the value of thermal conductivity of the alloys, for example, Touloukian et al. [34] reported a value of 216 W/mK for CuZr alloy while Yamasaki et al. [35] obtained 5.02 W/mK for $Zr_{55}Cu_{30}Al_{10}Ni_5$. For the studied $Cu_{50}Zr_{50}$, $Cu_{49.5}Zr_{50}Co_{0.5}$ and $Cu_{49}Zr_{50}Co_1$ alloys we could not measure experimentally the thermal conductivity and experimental results are not available in the literature. For this reason, it was estimated using the rule of mixtures since they led to reasonable values close to 216 W/mK and even error value of 20 % would all result in an estimated surface temperature below the start of the austenitic transformation peak (Fig. 2).

Table 3. Properties of elements and alloys at RT and 100°C and estimated contact surface temperature as a function of load and temperature (RT and 100°C).

	Mechanical properties					Contact surface temperature (°C)		
	E (GPa)	ρ (Kg/m^3)	v*	K (W/mK)	C (Nm/KgK)	N5	10N	N15
	RT|100°C	RT|100°C	RT|100°C	RT|100°C	RT|100°C	RT|100°C	RT|100°C	RT|100°C
Cu	130[b]|112[g]	8930[c]|8890[c]	0.34[b]	400[c]|395[c]	385[c]|397[c]	-	-	-
Zr	68[b]|62[g]	6520[e]|6488[e]	0.34[b]	21[d]|20[d]	285[d]|295[d]	-	-	-
Co	209[h]|187[g]	8862[c]|8827[c]	0.31[h]	99[c]|89[c]	424[c]|452[c]	-	-	-
Steel disk	210[i]|187[g]	8020[c]|8000[c]	0.29[i]	15[c]|16[c]	480[c]|500[c]	-	-	-
$Cu_{50}Zr_{50}$	99[a]|87[a]	7725[a]|7689[a]	0.34[a]	216[f]|224[f]	335[a]|346[a]	37[a]|117[a]	90[a]|120[a]	81[a]|153[a]
$Cu_{49.5}Zr_{50}Co_{0.5}$	99[a]|87[a]	7725[a]|7689[a]	0.34[a]	216[f]|224[f]	335[a]|346[a]	40[a]|122[a]	66[a]|125[a]	78[a]|154[a]
$Cu_{49}Zr_{50}Co_1$	100[a]|88[a]	7724[a]|7688[a]	0.34[a]	216[f]|224[f]	335[a]|347[a]	39[a]|118[a]	68[a]|139[a]	81[a]|155[a]

[a] Material properties (calculated)
[b] [V.M. Villapún, J. Medina, P. Pérez, F. Esat, F. Inam, S. González. Strategy for preventing excessive wear rate at high loads in bulk metallic glass composites. Materials and Design 135 (2017) 300-308]
[c] [Mills, K.C., 2002. Recommended values of thermophysical properties for selected commercial alloys. Woodhead Publishing.]
[d] [Fink, J.K. and Leibowitz, L., 1995. Thermal conductivity of zirconium. Journal of Nuclear Materials, 226(1-2), pp.44-50.]
[e] [Valencia, J.J. and Quested, P.N., 2013. Thermophysical properties]

[f] [Touloukian, Y.S., 1970. Thermal conductivity-metallic elements and alloys. Thermophysical properties of matter, 1, 985-987]
[g] [Courtney, T.H., 2005. Mechanical behavior of materials. Waveland Press.]
[h] [G.V. Samsonov (Ed.) in Handbook of the physicochemical properties of the elements, IFI-Plenum, New York, USA, 1968.]
[i] Engineering Properties of Steels, Philip D. Harvey, editor, American Society for Metals, Metals Park, OH, (1982).
[*] Poisson's ratio variation with form RT to 100°C is very small that makes it insignificant in terms of temperature estimation.

3.5. Oxidation

Fig. 7 and Fig. 8 show backscattered SEM images of the oxide layer for $15NCo_0RT$ and $15NCo_0100^oC$, respectively. The tonality of the oxide layer differs from the substrate due to the different atomic mass of elements. Also, the oxide layer is split into different layers of darker/brighter tonalities indicating that the nature of each layer is different from one another. In order to investigate the formation of oxides on the worn surface of the samples tested at $15NCo_0RT$ and $15NCo_0100^oC$ conditions, the cross-section of the samples have been investigated by backscattered and elemental mapping SEM analysis (Fig. 7 and Fig. 8).

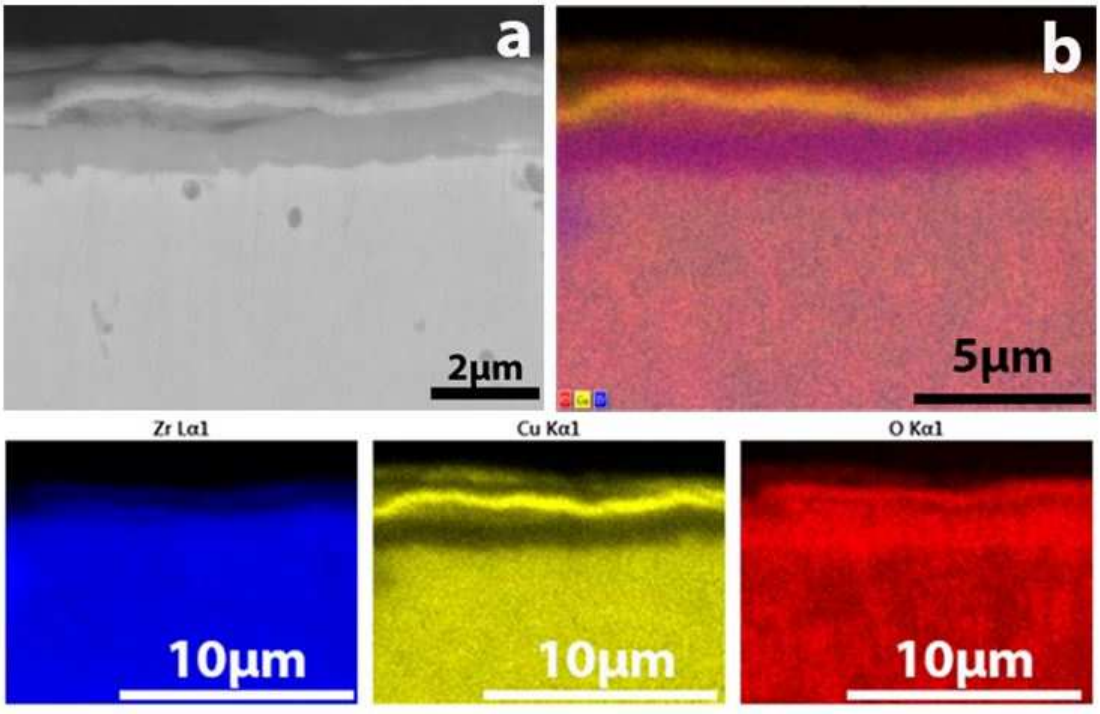

Fig. 7. a) Backscattered SEM and b) SEM-EDS elemental mapping for $15NCo_0RT$.

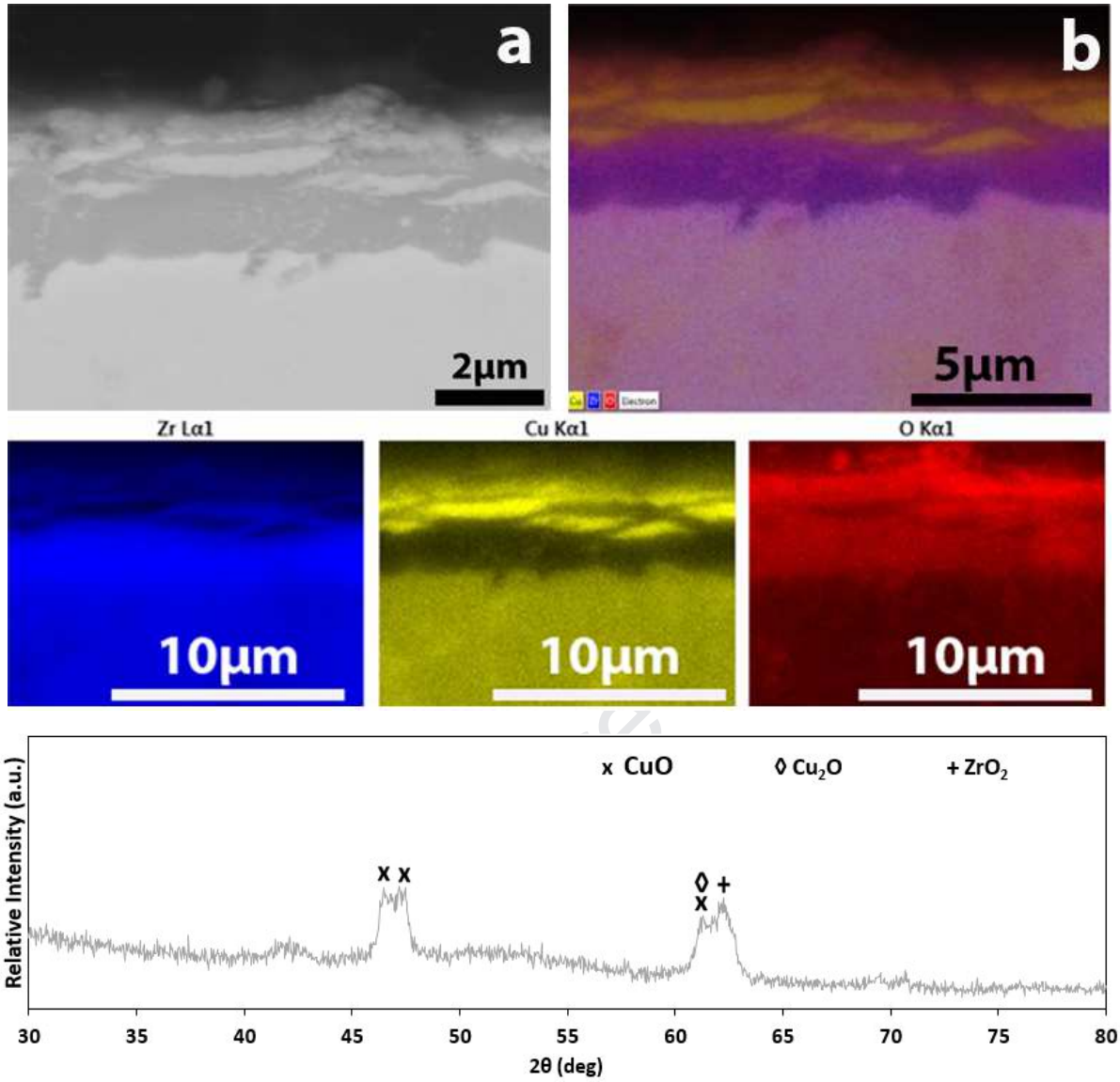

Fig. 8. a) Backscattered SEM, b) SEM-EDS elemental mapping for $15NCo_0100^oC$ along with the XRD scan from the top view (Fig. 4j).

For $15NCo_0RT$, the oxide layers are thinner than for $15NCo_0100^oC$. The backscattered image for $15NCo_0RT$ (Fig. 7) shows that the deepest oxide layer of dark tonality, in contact to the substrate is rich in Zr and oxygen with a composition of 25.81 at. % Zr, 17.94 at. % Cu and 56.26 at. % O and thus could be attributed to ZrO_2. The high propensity in the formation of ZrO_2 is consistent with the high negative enthalpy of mixing [36]. The second layer closer to the surface is of bright tonality and the concentration of Cu ranges from 49.66 to 67.48 at. % while for oxygen ranges from 20.44 to 28.80 at. % and thus could be attributed to Cu_2O. The outermost layer is of darker tonality and has similar ratio of Cu to oxygen and thus can be attributed to CuO. These same oxides have been detected by XRD from the

surface of the tested pins as shown in (Fig. 8c). For 15N$Co_0$100°C (Fig. 8) the composition of the oxide layers are very similar to those observed at RT and thus could be attributed to ZrO_2, Cu_2O and the outer layer to CuO. However, in this case, the Cu_2O layer is fractured into multiple fragments while for RT tests the fracturing is very limited and this can be attributed to the fact that the oxide layers at 100°C are thicker and thus the brittle oxide layer is more prone to be fractured than at RT. This is consistent with the Weibull modulus that describes the variability in the measured material strength [37], where under identical testing conditions, the failure of brittle specimens is related to the distribution of physical flaws and weak points, which is in this case the cracks and voids within the body of the oxide layer [38]. As the material wears out the ZrO_2 is formed again from the surface of the Cu_2O thus resulting in a multilayered-like structure. The Cu_2O fragments get more broken when closer to the surface, which could be expected due to the high shear forces during the test. As observed at 100°C, the oxide layer is thicker than at RT and thus more prone to get easily detached from the pin substrate, especially when subjected to shear stress [39, 40], which could be attributed to the mechanical stress generated between this oxide layer and the surface beneath [41]. The brittle oxides detached from the pin surface during the wear test can act as abrasive particles and therefore promote material removal from the pin thus resulting in higher mass loss, as observed at 100°C for 15 N load.

As mentioned in section 3.3, the dominant type of wear is abrasive, which is characteristic in shape memory alloys with high crystallinity [42] while the mechanism by which the material is removed is by displacement during ploughing process. On the worn surface, multiple features can be observed, including spot-like oxides, material transfer (see Fig. 5) and formation of a brittle oxide layer (see Fig. 7 and 8), these features play a major role in the evolution of mass loss.

Fig. 9 shows the roughness profile (arithmetic average: R_a) of the three alloys wear tested at 5, 10 and 15 N load at RT (Fig. 9a) and 100^{o}C (Fig. 9b).

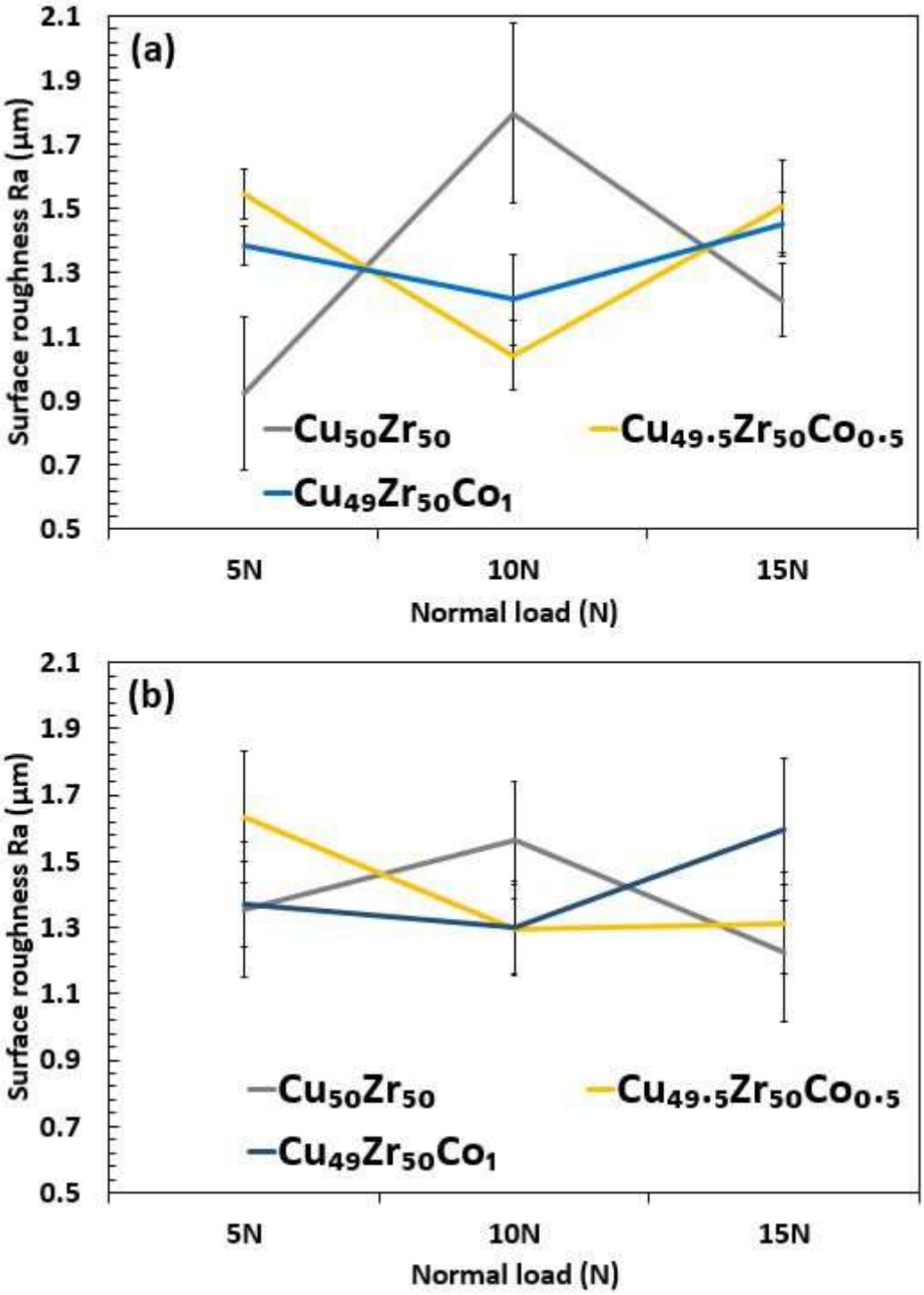

Fig. 9. Roughness profile of the $Cu_{50}Zr_{50}$, $Cu_{49.5}Zr_{50}Co_{0.5}$, and $Cu_{49}Zr_{50}Co_1$ alloys for 5, 10 and 15 N load applied a) at room temperature and b) at 100°C.

Two factors mostly determine the roughness profile and they are the following:

3.6.1. Oxidation

The roughness follow similar trend for $Cu_{50}Zr_{50}$, $Cu_{49.5}Zr_{50}Co_{0.5}$, and $Cu_{49}Zr_{50}Co_1$ at RT and 100°C. However, the average variation of roughness with load at RT is

higher (i.e., from 0.92 μm to 1.8 μm) than for 100°C (i.e., from 1.3 μm to 1.6 μm) due to the excessive oxidation effect at 100°C that tends to mask the changes taking place on the underlying substrate.

3.6.2. Martensitic transformation

For either austenite or martensite, an increase in load results in an increase of surface roughness because the removal of material increases with the increase of load. However, when the transition load (i.e., stress) for which austenite transforms into martensite is reached, the surface roughness drops rapidly since martensite is harder than austenite and thus martensite cannot be worn out so easily.

Since the trend for RT and 100^{o}C is similar but more noticeable at RT, the discussion will be only done for RT (see Fig. 9a). For $Co_{50}Zr_{50}$, R_a increased from 0.92 μm (for 5NCo_0RT) to 1.8 μm (for 10NCo_0RT) and then decreased to 1.22 μm, this could be attributed to martensitic transformation having a clear effect in limiting mass loss at 15N load. In this case, 10N load was not high enough to transform B2-austenite into B19-martensite. These findings are in agreement with the mass loss results (see Fig. 3a) where mass loss increase from 10N to 15N is less dramatic than from 5N to 10N. For the Co-containing alloys, the mass loss increase (Fig. 3a) from 5N to 10N for $Co_{0.5}$ and Co_1 is clearly lower than that for Co_0 indicating that martensitic transformation is already taking place at 10N. This happens because addition of Co promotes martensitic transformation and thus decreases the load required to initiate the transformation [9]. However, once the transformation has taking place, further increase in load (i.e., at 15 N) results in further removal of material and thus the roughness increases.

3.6. SEM and TEM

In order to analyse the wear performance of the three different compositions tested at RT and at 100°C, the microstructure has been analysed under a SEM and TEM.

The backscattered SEM images of (Fig. 10) for $Cu_{50}Zr_{50}$, $Cu_{49.5}Zr_{50}Co_{0.5}$, and $Cu_{49}Zr_{50}Co_1$ alloys show that the microstructure for the parent alloy and with 1 at. % Co are very similar but different from the alloy with 0.5 at. % Co, which is consistent with the XRD scans.

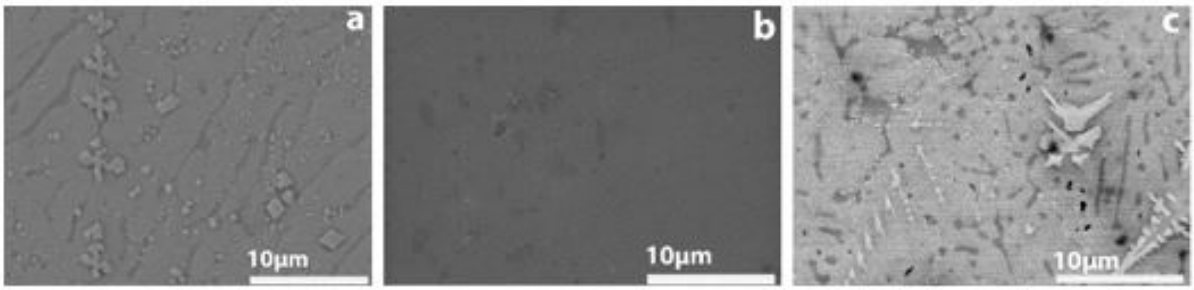

Fig. 10. Backscattered SEM images for as-cast a) $Cu_{50}Zr_{50}$, b) $Cu_{49.5}Zr_{50}Co_{0.5}$ and c) $Cu_{49}Zr_{50}Co_1$ alloys.

For Co_0 and Co_1 alloys the microstructure consists of clear tonality precipitates from about 1 μm (polygonal) to 5 μm (dendritic shape) size dispersed within a matrix of large dendrites of grey tonality surrounded by a dark phase at the interphases. From EDX, the composition of the precipitates range from 34.05-37.78 at. % Cu and 65.95-62.22 at. % Zr and therefore would correspond to $CuZr_2$. The composition of the dendrites is about 50.36-50.88 Cu and 49.12-49.64 at. % Zr, similar content of Cu and Zr and therefore would correspond to austenite/martensite. Finally, the approximate composition of the dark area between interphase could be associated to $Cu_{10}Zr_7$ at. % since the concentration of Cu and Zr ranges from 57.55-57.70 at. % Cu and 42.30-42.45 at. %, respectively. Considering that the microstructures are so fine that could not be easily identified by SEM, have performed TEM analysis. The microstructures for the three compositions are very similar as deduced from XRD (Fig. 1) and SEM (Fig. 10) and therefore we have focused our analysis on the $Co_{0.5}$ alloy since it exhibits the highest twinning propensity and thus lower mass loss. Fig. 11 shows a representative TEM images from the surface of the pin in contact with the steel disc after being tested at RT and 15 N load.

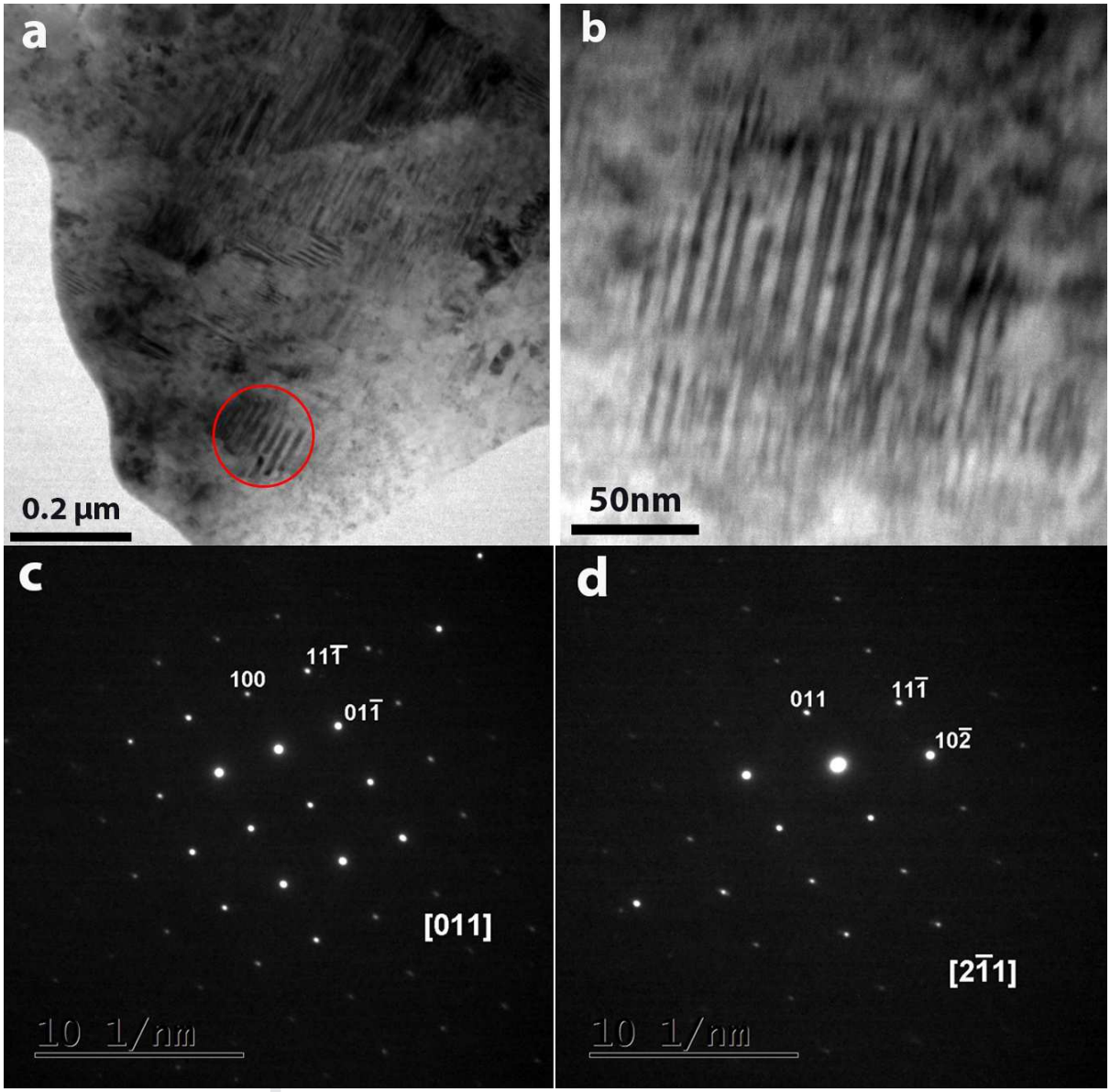

Fig. 11. (a) Bright field TEM image of $Cu_{49.5}Zr_{50}Co_{0.5}$ alloy tested at 15N and RT, (b) magnified twinned phase and (c) corresponding SAED patterns (B= [011] and B= [2-11]) of the B19' martensite twinned phase.

The microstructure consists of grains where most of them have a plate structure and about 0.2 µm size. EDX analysis from the highlighted circle in (Fig. 11a) indicate that the concentration of Cu ranges from 50.92 to 51.99 at. % and Zr from 46.32 to 47.51 at. % it therefore would correspond to $Cu_{50}Zr_{50}$ at. %. A magnified image of the grain inside the highlighted circle is shown in Fig. 11b, which has a clear twinned structure typical of martensite. To identify the nature of the crystalline phase, SAED patterns have been obtained. They can be effectively identified as [011] (Fig. 11c) and [2-11] (Fig. 11d) zone axes of B19' martensite phase respectively.

To understand the difference in performance when the samples are wear tested at 100°C, TEM images of the $Co_{0.5}$ sample at 15 N load have been studied. A representative area from the sample was shown in (Fig. 12).

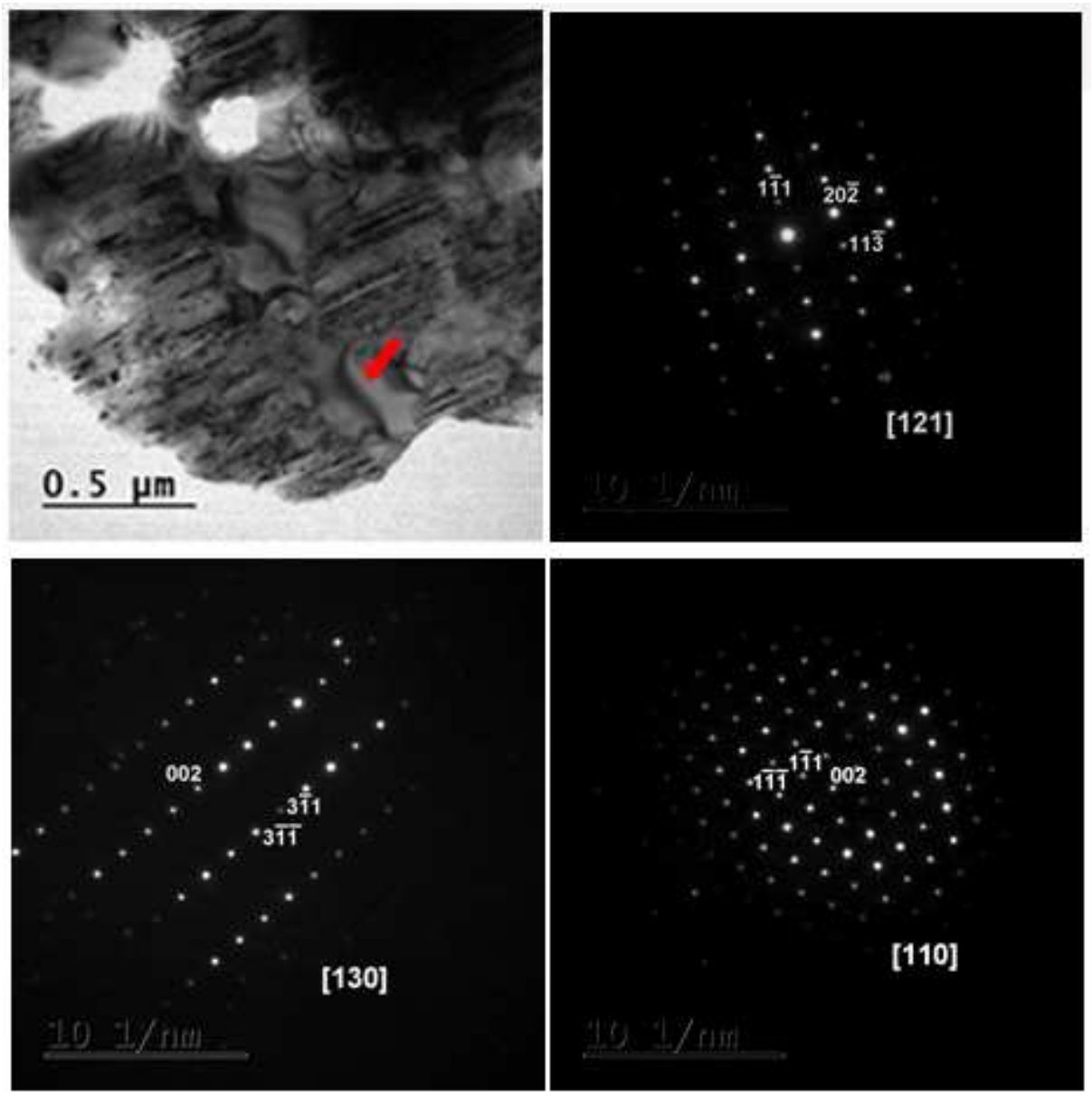

Fig. 12. (a) Bright field TEM image of $Cu_{49.5}Zr_{50}Co_{0.5}$ alloy tested at 15N and 100°C, (b, c and d) SAED patterns (B= [121], B= [130] and B= [110] respectively) of a grain without stripes corresponding to $Cu_{10}Zr_7$ (see red arrows).

Although some twinned grains (Fig. 12a) are observed, larger areas do not contain twinned grains as shown in the representative image of (Fig. 12a and 13) show that the microstructure consists of grains with plate structure and they have similar concentration of Cu and Zr and small Co content. Grains without stripes (see red

arrow) of 59 at. % Cu, 41 % at. Zr could be associated to the intermetallic $Cu_{10}Zr_7$ as can be proven from the SAED patterns of Fig. 11b, c and d.

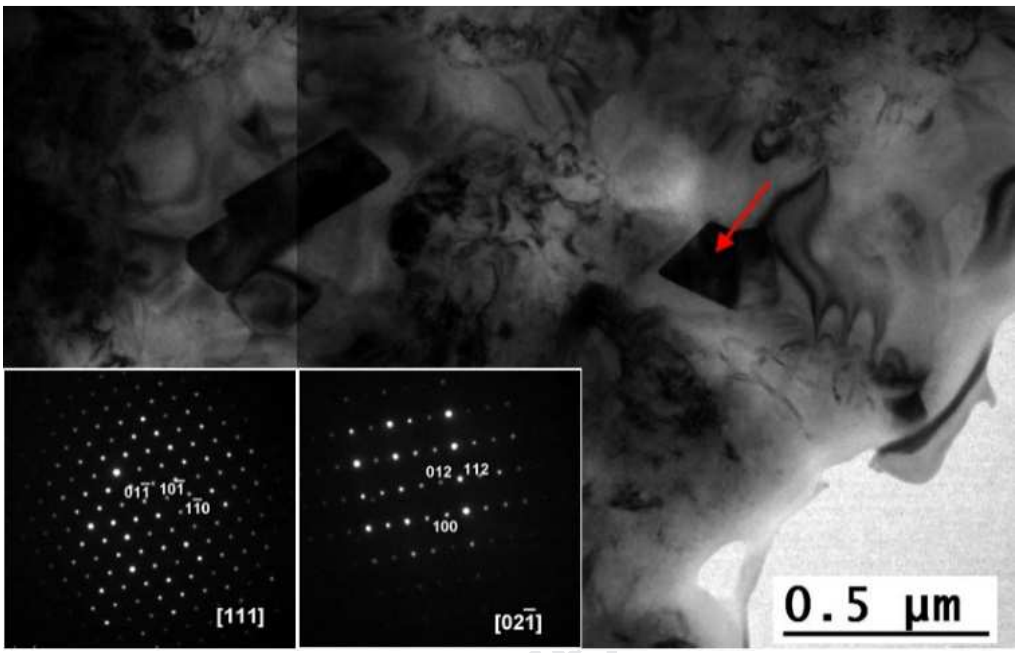

Fig. 13. (a) Bright field TEM image of $Cu_{49.5}Zr_{50}Co_{0.5}$ alloy tested at 15 N and 100°C. Inset: SAED patterns (B= [111] and B= [02-1]) of a trapezoidal shape particle (red arrow).

In order to assess the volume fraction of the crystalline phases present and considering the limitations of TEM (i.e., local technique), the analysis has been done from XRD results (Fig. 6). After testing with 15 N load at 100°C for 1 h (Fig. 6b), the intensity of the austenite peak increases indicating the volume fraction of austenite has increased due to an isothermal effect. In fact, volume fraction of austenite to martensite for as cast sample (Fig. 6a) is 1.4:1 and after testing at 100°C (Fig. 6b) is 2.6:1. Additionally, after annealing at 400°C (Fig. 6c) volume fraction of austenite to martensite is 7.1:1.

In addition, Cu-rich particles of different morphologies, including trapezoidal shape (see red arrow in Fig. 13) particles are present. These particles have a concentration of Cu ranging from 83.52 to 88.01 at. %, Zr from 7.22 to 12.38 at. % and Co from 2.1 to 3.37 at. %, and thus could identified as Cu_8Zr_3 compound with Co in solid solution. Fig. 13 shows a bright field TEM image of the microstructure containing these particles and the corresponding SAED patterns of the one with trapezoidal shape, which confirm the existence of Cu_8Zr_3 particles. It can be noticed that due to their small size, these particles were not detected by SEM.

In summary, these results show that for tests performed at RT and 15 N load the microstructure consists of twinned grains of B19' martensite. However, when testing at 100°C and 15 N load, some of the grains are not twinned, which is consistent with (1 hour testing) partial isothermal transformation of martensite into austenite (Fig. 6b and Fig. 12). This manuscript shows that although microalloying with Co promotes the martensitic transformation and thus it is a good strategy to prevent high mass loss at room temperature (Fig. 3a), it is not very useful to prevent mass loss if the surface contact temperature is close to A_s (Fig. 3b). In this latter case, when testing at 100°C, the mass loss of the $Co_{0.5}$ and Co_1 alloys are very similar to the parent Co_0 alloy and it is about twice the mass loss of $Co_{0.5}$ and Co_1 at RT. Moreover, addition of Co shifts the A_s temperature from 256.3°C for Co_0 to 218.8°C for Co1 thus reducing the operating temperature range.

This manuscript highlights the importance and limitations when selecting microalloying elements to enhance the wear resistance of CuZr-based SMAs. An engineering component of $Cu_{50}Zr_{50}$ working at 100°C in friction contact with SS304 steel would exhibit about double mass loss (about half lifetime) than while working at RT. The outcomes of this manuscript could be useful for selecting Cu-Zr SMAs for engineering components and points out the need of using microalloying elements that can also extent the operating temperature (shifting A_s to higher temperatures) to prevent early failure associated to excessive mass loss.

4. Conclusions

In this manuscript, the effect of temperature on the tribological performance of CuZr-based SMA has been studied by investigating wear behaviour and mass loss of $Cu_{50}Zr_{50}$, $Cu_{49.5}Zr_{50}Co_{0.5}$ and $Cu_{49}Zr_{50}Co_1$ at RT and 100^{o}C. The combined effect of oxidation and martensitic transformation determined the overall mass loss achieved at 5, 10 and 15 N at RT and 100^{o}C and the following conclusions can be made:

- The Mass loss at RT is the lowest for $Co_{0.5}$ due to the effect of the microalloying element in promoting martensitic transformation (i. e., the material hardens).
- The mass loss at 100^{o}C is higher than at RT and similar for the three compositions (Co_0, $Co_{0.5}$ and Co_1) thus indicating that the martensitic transformation is not as effective as at RT. This could be attributed to the fact that the contact temperature is close to the start of the austenite peak and thus stress-

induced martensite partly reverts into austenite via an isothermal process (see Fig. 6). In addition, the material is more prone to oxidation and therefore it develops a thick oxide layer that tends to detach easily (Fig. 8) thus resulting in an increase of mass loss.

- Addition of a microalloying element, such as Co, which promotes the martensitic transformation, is a good strategy to improve the wear resistance at room temperature of CuZr-based alloys. However, it is not useful at 100°C and this could be partly improved by microalloying using elements that can shift the austenitic transformation peak A_s to higher temperatures to increase the operating temperature range (i.e., A_s-RT) to prevent the stress-induced martensite revert into soft (i.e., low wear resistant) austenite.
- This manuscript highlights through a critical analysis the importance of wise selection of microalloying elements in shape memory alloys since addition of an element that can effectively enhance the wear resistance at RT may decrease the operating temperature range to such an extent that for relatively low temperatures of 100°C, microalloying would have practically no benefit in enhancing the durability.

Acknowledgments

This work has been partially financed by EPSRC (EP/P019889/1) First Grant scheme S.G. and P.N. acknowledges research contract from EPSRC. A. Younes acknowledge research support from Northumbria University. J. Medina and P. Pérez would like to acknowledge the expert support of A. García and A. Tomás for assistance with SEM/TEM observations.

References

1. Jani, J.M., et al., *A review of shape memory alloy research, applications and opportunities.* Materials & Design (1980-2015), 2014. **56**: p. 1078-1113.
2. Van Humbeeck, J., *Shape memory alloys: a material and a technology.* Advanced engineering materials, 2001. **3**(11): p. 837-850.
3. Xie, J.-X., J.-L. Liu, and H.-Y. Huang, *Structure design of high-performance Cu-based shape memory alloys.* Rare Metals, 2015. **34**(9): p. 607-624.
4. Rahaman, M.L., L.C. Zhang, and H.H. Ruan, *Effects of environmental temperature and sliding speed on the tribological behaviour of a Ti-based metallic glass.* Intermetallics, 2014. **52**: p. 36-48.
5. Biffi, C.A., A. Figini, and A. Tuissi, *Influence of compositional ratio on microstructure and martensitic transformation of CuZr shape memory alloys.* Intermetallics, 2014. **46**: p. 4-11.

6. Rahaman, M.L. and L. Zhang, *On the estimation of interface temperature during contact sliding of bulk metallic glass.* Wear, 2014. **320**: p. 77-86.
7. Motemani, Y., et al., *Effect of cooling rate on the phase transformation behavior and mechanical properties of Ni-rich NiTi shape memory alloy.* Journal of Alloys and Compounds, 2009. **469**(1): p. 164-168.
8. Javid, F.A., et al., *Effect of Cobalt on Phase Formation, Microstructure, and Mechanical Properties of Cu50−xCoxZr50 (x = 2, 5, 10, 20 at. pct) Alloys.* Metallurgical and Materials Transactions A, 2012. **43**(8): p. 2631-2636.
9. Wu, Y., et al., *Ductilizing Bulk Metallic Glass Composite by Tailoring Stacking Fault Energy.* Physical Review Letters, 2012. **109**(24): p. 245506-1-245506-12.
10. Villapún, V.M., et al., *Antimicrobial and wear performance of Cu-Zr-Al metallic glass composites.* Materials & Design, 2017. **115**: p. 93-102.
11. Hattori, S. and A. Tainaka, *Cavitation erosion of Ti–Ni base shape memory alloys.* Wear, 2007. **262**(1): p. 191-197.
12. Villapún, V.M., et al., *Strategy for preventing excessive wear rate at high loads in bulk metallic glass composites.* Materials & Design, 2017. **135**: p. 300-308.
13. De Luca, F., et al., *Stress-induced martensitic transformation of Cu50Zr50 shape memory alloy optimized through microalloying and co-microalloying.* Journal of Alloys and Compounds, 2019. **781**: p. 337-343.
14. Zhou, D.Q., et al., *Alloying effects on mechanical properties of the Cu–Zr–Al bulk metallic glass composites.* Computational Materials Science, 2013. **79**: p. 187-192.
15. Jiang, S.-S., et al., *A CuZr-based bulk metallic glass composite with excellent mechanical properties by optimizing microstructure.* Journal of Non-Crystalline Solids, 2018. **483**: p. 94-98.
16. Ding, J., et al., *Large-sized CuZr-based Bulk Metallic Glass Composite with Enhanced Mechanical Properties.* Journal of Materials Science & Technology, 2014. **30**(6): p. 590-594.
17. Oliveira, J.P., et al., *Laser welding of Cu-Al-Be shape memory alloys: Microstructure and mechanical properties.* Materials & Design, 2018. **148**: p. 145-152.
18. Oliveira, J.P., et al., *Microstructure and mechanical properties of gas tungsten arc welded Cu-Al-Mn shape memory alloy rods.* Journal of Materials Processing Technology, 2019. **271**: p. 93-100.
19. Xu, S., et al., *Negative Poisson's ratio in Heusler-type Cu–Al–Mn shape memory alloy.* Scripta Materialia, 2020. **177**: p. 74-78.
20. González, S., et al., *Drastic influence of minor Fe or Co additions on the glass forming ability, martensitic transformations and mechanical properties of shape memory Zr–Cu–Al bulk metallic glass composites.* Science and Technology of Advanced Materials, 2014. **15**(3): p. 035015.
21. Jiang, Q.K., et al., *Glass formability, thermal stability and mechanical properties of La-based bulk metallic glasses.* Journal of Alloys and Compounds, 2006. **424**(1): p. 183-186.
22. Nishiyama, N., K. Amiya, and A. Inoue, *Novel applications of bulk metallic glass for industrial products.* Journal of Non-Crystalline Solids, 2007. **353**(32): p. 3615-3621.
23. Cui, X., et al., *Study of the reversible intermetallic phase: B2-type CuZr.* Intermetallics, 2013. **36**: p. 21-24.
24. Wu, Y., et al., *Formation of Cu–Zr–Al bulk metallic glass composites with improved tensile properties.* Acta Materialia, 2011. **59**(8): p. 2928-2936.
25. Bhushan, B., *Modern Tribology Handbook, Two Volume Set*. 2000: CRC Press p. 235-272.
26. Wei, Y.X., et al., *Erbium- and cerium-based bulk metallic glasses.* Scripta Materialia, 2006. **54**(4): p. 599-602.
27. Mills, K.C., *Recommended Values of Thermophysical Properties for Selected Commercial Alloys*. 2002: Woodhead Publishing p. 73-134.

28. Fink, J.K. and L. Leibowitz, *Thermal conductivity of zirconium.* Journal of Nuclear Materials, 1995. **226**(1): p. 44-50.
29. Valencia, J.J. and P.N. Quested, *Thermophysical properties.* ASM Handbook, 2008. **15**: p. 468-481.
30. Samsonov, G.V., *Handbook of the Physicochemical Properties of the Elements*. 1st ed. 1968: Springer US p. 395-396.
31. Harvey, P.D. and A.S.f. Metals, *Engineering properties of steel*. 1982: American Society for Metals p. 259-270.
32. Courtney, T.H., *Mechanical Behavior of Materials*. 2nd ed. 2005: Waveland Press p. 50-59.
33. Spittel, T. and M. Spittel, *Ferrous Alloys*. 1st ed. Vol. 2. 2009: Springer-Verlag Berlin Heidelberg p. 1-3.
34. Touloukian, Y.S., *Thermal Conductivity-Metallic Elements and Alloys*. Thermophysical Properties of Matter. Vol. 1. 1970: IFI/Plenum p. 985-987.
35. Yamasaki, M., S. Kagao, and Y. Kawamura, *Thermal diffusivity and conductivity of Zr55Al10Ni5Cu30 bulk metallic glass.* Scripta Materialia, 2005. **53**(1): p. 63-67.
36. Boer, F.R.d., et al., *Cohesion in metals*. 1988, Netherlands: North-Holland p. 751-755.
37. Zhao, Y.-Y., E. Ma, and J. Xu, *Reliability of compressive fracture strength of Mg–Zn–Ca bulk metallic glasses: Flaw sensitivity and Weibull statistics.* Scripta Materialia, 2008. **58**(6): p. 496-499.
38. Zberg, B., et al., *Tensile properties of glassy MgZnCa wires and reliability analysis using Weibull statistics.* Acta Materialia, 2009. **57**(11): p. 3223-3231.
39. Ji, X., S.H. Alavi, and S.P. Harimkar, *High-Temperature Sliding Wear Behavior of Zr-Based Bulk Amorphous Alloys.* JOM, 2015. **67**(7): p. 1578-1584.
40. González, S., et al., *Effect of thermally-induced surface oxidation on the mechanical properties and corrosion resistance of Zr 60 Cu 25 Al 10 Fe 5 bulk metallic glass.* Science of Advanced Materials, 2014. **6**(1): p. 27-36.
41. William, B.A., C. Margam, and L.N. Lam, *Materials Degradation And Its Control By Surface Engineering*. 2nd ed. 2003: World Scientific Publishing Company p. 119-126.
42. Liu, Y., et al., *Wear behavior of a Zr-based bulk metallic glass and its composites.* Journal of Alloys and Compounds, 2010. **503**(1): p. 138-144.

Highlights:

- Study the effect of microalloying using cobalt on the wear rate at room temperature and 100°C for $Cu_{50}Zr_{50}$ SMA.
- Maximum wear resistance is achieved for the alloy with 0.5 at. % Co at room temperature.
- The wear resistance decreases at 100°C due to partial isothermal transformation into austenite and excessive oxidation.

Author contribution sections

Authors contributions: S.G. and A.Y. designed research; A.Y., P.N., J.M., P.P, V.M., F.B. performed research; S.K, E.J analysed data; A.Y. and S.G. wrote the paper

Declaration of interests

☒ The authors declare that they have no known competing financial interests or personal relationships that could have appeared to influence the work reported in this paper.

☐The authors declare the following financial interests/personal relationships which may be considered as potential competing interests: